Effect of sputter heating in ionized metal physical vapor deposition reactors

Junqing Lu[a)]
Department of Mechanical and Industrial Engineering, University of Illinois, 1406 West Green Street, Urbana, Illinois 61801

Mark J. Kushner[b)]
Department of Electrical and Computing Engineering, University of Illinois, 1406 West Green Street, Urbana, Illinois 61801

(Received 22 October 1999; accepted for publication 10 February 2000)

Ionized metal physical vapor deposition (IMPVD) is a process in which sputtered metal atoms from a magnetron target are ionized by a secondary plasma, accelerated into the substrate, and deposited with moderately anisotropic fluxes. The momentum and energy transfer from the sputtered metal atoms and ion-produced reflected neutrals to the background gas, sputter heating, produces rarefaction which influences the operating characteristics of the discharge. To address these processes, a model was developed to simulate the sputtering of metal atoms and their transport in IMPVD reactors. The model accounts for the ion-energy-dependent yield and kinetic energy of the sputtered and reflected atoms, and for sputter heating. The model was validated by comparing its results to experimentally measured metal atom densities and the ionization fraction of the deposition flux. Sputter heating as a function of auxiliary ionization and magnetron power in an inductively coupled plasma IMPVD reactor for Al deposition was then investigated. Sputter heating produces rarefaction of the buffer gas which results in a redistribution of Al species in the reactor compared to the absence of sputter heating. Consequently, the ionization fraction of the depositing metal flux decreases, while the magnitude of the flux increases. The minimum Ar density due to sputter heating is regulated by heat transfer to the target. The electron density increases significantly with the addition of a small amount of metal atoms to the plasma. © *2000 American Institute of Physics*. [S0021-8979(00)04410-8]

I. INTRODUCTION

The ionized metal physical vapor deposition (IMPVD) process is being developed to deposit metals into trenches and vias of high aspect ratio for interconnects[1–8] and for deposition of seed layers and diffusion barriers[3] in the fabrication of integrated circuits. In IMPVD, physical sputtering, usually from a magnetron cathode, produces a flux of metal atoms toward the substrate. A secondary plasma, typically an inductively coupled plasma (ICP), is produced between the target and the substrate by a radio-frequency (rf) driven antenna. The plasma is usually sustained in an inert gas such as Ar or Ne at moderate pressures of tens of mTorr to slow down the sputtered atoms and ionize them prior to their reaching the substrate. Typical ionization fractions of the metal are from tens of a percent to as large as 90%.[1] A rf bias may be applied to the substrate to vertically accelerate the metal ions into the wafer. A combination of anisotropic metal atoms and isotropic neutral metal atoms results in conformal deposition and prevents pinchoff[1] when filling trenches.

The kinetic energy of the sputtered metal atoms from the cathode is on the order of several electron volts, while the kinetic energy of the background gas atoms is less than 0.1 eV. In addition, the ions which are incident on the target have energies of hundreds of eV, and are reflected as neutral atoms which also have kinetic energies of several eV. Power transferred from the sputtered metal atoms and the reflected neutrals to gas atoms during collisions produces ''sputter heating'' and ultimately rarefaction of the gas. This gas heating and subsequent rarefaction have been observed in various experiments. For example, in measurements in a magnetron using a directional pressure probe, Hoffman[4] found that the gas density decreased by as much as 10% at pressures of tens of mTorr and currents of 12 A, an effect attributed to sputter heating.

Rossnagel[6] measured gas pressures as a function of magnetron power, cathode material, and type of buffer gases in a magnetron reactor having a secondary ICP. His results indicated that the gas density in front of the magnetron was significantly reduced as the magnetron power increased. For example, the gas density decreased by 40% when the magnetron power was increased from 0.5 to 2.0 kW at an Ar pressure of 30 mTorr with 600 W ICP power and a Cu target. The rarefaction saturated with magnetron current, and increased with the sputter yield of the cathode and gas collision cross section.

Dickson *et al.*[7,8] measured electron temperature, electron densities, metal deposition rates, and optical emission for Al IMPVD. The electron temperature and line integrated electron density decreased as the magnetron current increased at Ar pressures of 10 and 30 mTorr and 200 W ICP power. Predicted electron densities from a global model[7] agreed

a)Electronic mail: j-lu@uiuc.edu
b)Electronic mail: mjk@uiuc.edu

well with the measured densities when the gas temperature was increased from 350 to 890 K as the magnetron current was increased from 0 to 1.2 A, suggesting that the decrease in electron density was correlated with sputter heating. From the deposition rates and emission intensities, Al and Al^+ densities were obtained for 400 W ICP and 240 W magnetron at 30 mTorr Ar.[8] The Al density monotonically decreased from $10^{12}\,cm^{-3}$ below the target to about $10^{11}\,cm^{-3}$ at 8 cm below the target, while the Al^+ density was maximum near the center of the reactor, and was on the order of $10^{10}\,cm^{-3}$ in the entire region between the target and the substrate.

Using a Monte Carlo simulation, Turner[9] investigated the consequences of background gas, pressure, discharge voltage, current, and cathode–substrate separation on the gas temperature in a dc magnetron discharge. At constant pressures (7.5 and 30 mTorr) and high discharge currents (0.2–20 A), the maximum gas temperature varied from 500 to 5000 K, and was proportional to the square root of the current. At constant pressure, the temperature increased linearly with the cathode–substrate separation since sputtered and reflected atoms are increasingly more likely to have collisions with the background gas atoms rather than with the walls. The magnitude of heating depended strongly on the cathode material. Higher sputter yields produced more sputtered atoms and more sputter heating.

Serikov and Nanbu[10] developed a particle-in-cell/Monte Carlo model for gas heating in a dc discharge for Al and Cu targets at an Ar pressure of 42 mTorr. The predicted gas heating for the Cu target was larger than that for the Al target because the sputter yield for Cu is twice that for Al. The gas temperature at the center of the plasma was 330 and 460 K for discharge voltages of 300 and 1500 V. The gas temperature was a sensitive function of the thermal accommodation coefficient for the reflected neutrals from the target. At a target bias of -1500 V, the maximum gas temperature increased from 350 to 460 K when the accommodation coefficient was decreased from 1.0 to 0.75.

In this article, we present results from a modeling study of sputter heating in an IMPVD reactor having an aluminum target. The computational platform used in this study is the two-dimensional Hybrid Plasma Equipment Model (HPEM).[11,12] The consequences of magnetron power and ICP power on gas heating were investigated. It was found that the Al species were redistributed in the reactor due to the gas rarefaction caused by sputter heating. As a result, the ionization fraction of the depositing Al flux decreased, and the magnitude of the depositing flux increased, akin to operating at a lower gas pressure. It was also found that the electron density increased significantly with the addition of a small amount of metal atoms to the plasma. The model will be described in Sec. II, followed by a discussion of validation in Sec. III and sputter heating processes in Sec. IV. Our concluding remarks are in Sec. V.

II. DESCRIPTION OF THE MODEL

The modeling platform used in this study is the HPEM which has been described in detail in previous publications.[11,12] The HPEM is a modular simulation which iteratively achieves a quasisteady state solution. The modules used here are the electromagnetic module (EMM), the electron energy transport module (EETM), and the fluid kinetics simulation (FKS). Inductively coupled electric and magnetic fields are computed in the EMM. These fields are then used in EETM to solve the electron energy equation for the temperature of bulk electron and, using Monte Carlo techniques, the trajectories and distribution functions of secondary electrons emitted from the cathode. The electron temperatures and energy distributions are used to compute source rates for electron impact processes and electron transport coefficients. These rates and coefficients are then used in the FKS where continuity, momentum, and energy equations are solved for all heavy particles (neutrals and ions). Poisson's equation is solved for the plasma potential throughout the reactor. Sheaths at the target and substrate are resolved using a semianalytic sheath model[12] for both rf and dc sheaths. The sputter transport and heating algorithms, described below, are included in the FKS. Densities and electric fields are then transferred to the EMM and EETM, and the process is repeated until a converged solution is obtained. The gas pressure was held constant at the specified value by throttling the pump rate. The electron motion in radial and axial directions is resolved within each rf period. The electron motion in the azimuthal direction is not resolved in the fluid modules, but is tracked in the Monte Carlo modules. The electron energy and density shown here are averaged over several rf periods.

To address sputter heating, improvements were made to the sputtering and sputtered atom transport algorithms. Ion-energy-dependent yields of sputtered atoms are now obtained from a semiempirical relationship whose parameters are determined from experimental data[13,14] and which is valid for monatomic ion–target pairs. The sputter yield for ions of energy E_i is[13]

$$Y(E_i)=\begin{cases} 0.42\dfrac{\alpha Q K s_n(\epsilon)}{U_s[1+0.35U_s s_e(\epsilon)]}(1-\sqrt{E_{th}/E_i})^{2.8}, \\ \quad E_i > E_{th} \\ 0, \quad E_i \leqslant E_{th}, \end{cases} \tag{1}$$

where E_{th} is the threshold energy and ϵ is the reduced energy, a function of atomic numbers and masses. Q and α are empirical parameters, and U_s is the surface binding energy in eV. s_n and s_e are Lindhard's reduced cross sections[13,15] for elastic (loss of energy to atomic recoils) and inelastic (loss of energy to electrons) stopping. K is a factor to convert Lindhard's elastic stopping cross section S_n to the reduced stopping cross section s_n. E_{th}/U_s and α are dependent on the mass ratio M_t/M_i (t and i indicate target atom and incident ion, respectively), while Q depends only on the atomic number of the target atom. The yield is proportional to the elastic stopping cross section, and decreases as the surface binding energy increases. The yield also decreases when the momentum of the incoming ion is transferred to the electronic mode. E_{th} is proportional to U_s and is about 30 eV for Al. The parameters used here for the Ar^+–Al sputter pair

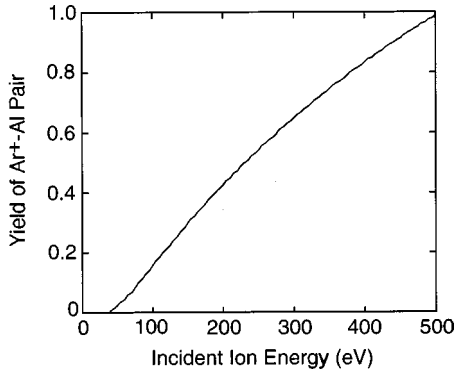

FIG. 1. Sputter yield for Ar^+–Al pairs calculated from the semi-empirical formula. The yield increases linearly with incident Ar^+ energy up to hundreds of eV.

were $\alpha=0.23$, $Q=1.1$, and $U_s=3.4\,\mathrm{eV}$. The yield for Ar^+–Al pairs using these parameters is shown in Fig. 1. To first order, the yield increases linearly with the ion energy up to hundreds of eV, producing a yield of 0.43 at 200 eV.

The kinetic energy of the emitted atoms is given by Thompson's theory of atomic collision cascades[16] for incoming ions of moderate energy (hundreds of eV). The normalized cascade distribution is[17,18]

$$F(E)=\begin{cases} 2\left(1+\dfrac{U_s}{\Lambda E_i}\right)^2 \dfrac{U_s E}{(U_s+E)^3} & \text{for } E\leqslant \Lambda E_i, \\ 0 \quad \text{for } E>\Lambda E_i \end{cases}, \tag{2}$$

where E is the kinetic energy of the sputtered atom, ΛE_i is the maximum recoil energy, and $\Lambda=4M_iM_t/(M_i+M_t)$. The random sampling of E from $F(E)$ is performed by the inverting the distribution,

$$\int_0^E F(E')dE'=r, \tag{3}$$

where r is a random number in the interval [0,1]. The energy of the sputtered atom[14] is then

$$E=\frac{U_s\Lambda E_i\sqrt{r}}{U_s+\Lambda E_i(1-\sqrt{r})}. \tag{4}$$

The Thompson distribution peaks at half the surface binding energy. Due to the high-energy tail of the distribution, the average energy of the sputtered Al atoms is generally several eV. Under the operating conditions of interest, the sheath thickness is small compared to the ion mean free path, and the dc sheath at the target is essentially collisionless. Hence, the kinetic energy of the incoming ion is equal to the sheath potential, which is computed in the semianalytical sheath model.[12]

The energies of the reflected Ar neutral atoms from Ar^+ incident on surfaces were obtained from TRIM simulations as a function of ion energy.[19,20] The average energy of the reflected Ar neutrals was curve fitted into a thermal accommodation coefficient α_T as a function of incident ion energy,

$$\alpha_T=\frac{E_i-E_r}{E_i-E_T}, \tag{5}$$

where E_r is the kinetic energy of the reflected neutrals, and E_T is the kinetic energy of the reflected neutrals in thermal equilibrium with the target at 350 K. Under typical operating conditions, $\alpha\approx 0.95$. Since the energy distribution of the reflected neutrals is not monoenergetic, but also has a thermal component, it was assumed that 90% of the incident Ar ions are reflected with energy E_r and 10% are reflected thermally. Based on results of molecular dynamics simulations, it was assumed that 25% of the incident Al ions on the target are reflected thermally as neutrals, whereas 75% of the incident Al ions deposit. (Approximately 90% of the incident ions are Ar^+.) The transport of the reflected neutrals in the background gas is modeled in the same manner as the sputtered atoms.

The transport of the sputtered and reflected atoms is handled by a Monte Carlo simulation where they are represented by computational pseudoparticles. Each pseudoparticle carries a ''weighting'' which is used to determine its contributions to momenta, energy, and density in collisions with bulk gas atoms. The weighting of the ith sputtered atom is

$$W_i=\frac{Y[E_i(\mathbf{r})]\Phi(\mathbf{r})A(\mathbf{r})}{N(\mathbf{r})V(\mathbf{r})}, \tag{6}$$

where Y is the energy-dependent yield of the target, $E_i(\mathbf{r})$ is the incident ion energy at target location $\mathbf{r}$, Φ is the flux of ion and fast neutrals to the target (fast neutrals and ions of the same energy are considered equivalent with respect to sputtering), N is the number of Monte Carlo particles released from that location, and A is the surface area of the computational cell on the target. V is the volume of the computational cell at $\mathbf{r}'$ where the collision occurs.

The sputtered and reflected neutral atoms are emitted from the target surface with angles having a cosine distribution.[21] Monte Carlo techniques are then used to follow the trajectories of the emitted atoms. The mean free path of the sputtered atom is determined using null collision techniques[17] to account for spatially dependent gas properties (density and composition) that may occur as a consequence of both rarefaction and slowing of sputtered atoms. Collisions with gas atoms exchange only translational energy (electronic excitation is ignored).

Statistics are collected on the velocities of Monte Carlo particles before and after collisions to determine the net momentum and thermal energy transfer to the gas. The rate of change in momentum for the background gas atom (denoted by subscript g) after the collision is

$$\frac{d}{dt}(n_g\Delta\mathbf{v}_g)=\frac{Wm_s}{m_g}(\mathbf{v}_s'-\mathbf{v}_s), \tag{7}$$

where $\mathbf{v}_s$ is the velocity after the collision, $\mathbf{v}_s'$ is its velocity before the collision, m is the mass of the atoms, subscript s denotes sputtered atoms, and W is the appropriate weighting for the sputtered atoms, defined in Eq. (6). The change in the background gas velocity is averaged over all collisions with the sputtered atoms, and the contribution is added as a source term to the momentum equation for the bulk fluid.

The conservation of both momentum and energy is problematic since scattering of the kinetically tracked sputtered

atoms occurs in three dimensions whereas momentum and energy are transferred to a background gas which is represented by fluid equations in two dimensions (r, z). The random thermal energy transferred to the background gas is obtained by subtracting the directional kinetic energy from the total change in kinetic energy of the background gas atom after the collision. For example, consider collecting statistics on two collisions, with an increment in kinetic energy in the positive and negative radial directions of 1 and 2 (arbitrary units). The total increment in kinetic energy is 3. However, the directional kinetic energy which can be resolved in the momentum equation is only 1. The remaining energy is considered ''random'' and is handled as a contribution to the energy equation.

The sputtered atoms that slow down to thermal speeds in the Monte Carlo simulation are recorded in a Green's function, which is then used as a source term in the fluid continuity equations. The Green's function is

$$G(\mathbf{r},\mathbf{r}')=\sum_i \frac{Y[E_i(\mathbf{r})]A(\mathbf{r})}{N(\mathbf{r})V(\mathbf{r}')}\delta(\mathbf{r}',\mathbf{r}_i'), \tag{8}$$

where the sum is over all atoms sputtered from the target at location $\mathbf{r}$, and the sputtered atom slows to thermal speeds at location $\mathbf{r}_i'$. The contribution to the species density n at $\mathbf{r}'$ is then

$$\frac{dn(\mathbf{r}')}{dt}=\sum_j \Phi(\mathbf{r}_j)G(\mathbf{r}_j,\mathbf{r}'), \tag{9}$$

where the sum is over all target locations j. The in-flight metal atoms, that is, those sputtered metal atoms with velocities above thermal speed, are recorded in a separate Green's function.

The Ar/Al chemistry used in this study is shown in Table I. The majority of the reactions belong to either electron–impact reactions or charge–exchange reactions. The e/Ar chemistry includes electron impact excitation of Ar from ground state to excited states $4s$ and $4p$ (which are lumped into Ar*) and electron impact ionization (from the Ar ground state and Ar*). The e/Al chemistry includes electron impact excitation of Al from the ground state to excited states $4s$, $3p$, $3d$, and $4p$ (which are lumped into Al*), superelastic collision to de-excite Al* to the ground state, and electron impact ionization (from the Al ground state and Al*). Electron impact excitation cross sections for Al are not readily available. Hence, the Al excitation cross sections are estimated from plane-wave Born approximation calculations.[22] The Al* is quenched by collisions with Al, Al*, and Ar, although its de-excitation is dominated by radiative relaxation. The Ar* reacts with Ar* to produce Ar^+, and with Al or Al* to produce Al^+ through Penning processes. Charge exchange reactions play an important role in generating fast neutral fluxes to the target and ionizing Al atoms before they reach the substrate. The reaction rates for charge exchange are large, approximately $10^{-9}\,cm^{-3}\,s^{-1}$. This value is somewhat an upper limit. The change in gas species density is less than 10% for a 50% decrease in the charge–exchange reaction rates. The charge–exchange reactions include resonant exchange among the Ar species or the Al species and nonresonant exchange between Ar and Al species. These Ar/Al heavy body reaction rates are estimated based on Ar/Cu heavy body reaction rates.[12] There is enough similarity between the Ar/Al and the Ar/Cu chemistry to warrant such an estimate. The charge–exchange reactions generate energetic neutrals, which significantly contribute to heating of the buffer gas.[10] Heavy particle cross sections for gas heating from the elastic collisions between the sputtered and reflected neutrals and the background gas are computed from Lennard-Jones radii.

TABLE I. Ar/Al chemistry.

Reaction[a]	Rate coefficient ($cm^{-3}\,s^{-1}$)	Reference
$e+Ar\rightarrow Ar+e$	b	22
$e+Ar\rightarrow Ar(4s)+e$	b	23
$e+Ar\rightarrow Ar(4p)+e$	b	23
$e+Ar\rightarrow Ar^++e+e$	b	24
$e+Ar^*\rightarrow Ar^++e+e$	b	25
$e+Ar^*\rightarrow Ar+e$	c	23
$e+Al\rightarrow Al(4s)+e$	b	26
$e+Al\rightarrow Al(3p^2)+e$	b	26
$e+Al\rightarrow Al(3d)+e$	b	26
$e+Al\rightarrow Al(4p)+e$	b	26
$e+Al\rightarrow Al^++e+e$	b	27
$e+Al^*\rightarrow Al^*+e$	b	28
$e+Al^*\rightarrow Al+e+e$	b	28
$e+Al^*\rightarrow Al+e$	c	26
$Al^*\rightarrow Al$	7.3×10^{5}	d
$Ar^*+Ar^*\rightarrow Ar^++Ar+e$	5.0×10^{-10}	d
$Al^*+Al\rightarrow Al+Al$	1.0×10^{-12}	d
$Al^*+Al^*\rightarrow Al+Al$	1.0×10^{-12}	d
$Al^*+Ar\rightarrow Al+Ar$	1.0×10^{-12}	d
$Ar^*+Al\rightarrow Al^++Ar+e$	5.9×10^{-10}	d
$Ar^*+Al^*\rightarrow Al^++Ar+e$	5.9×10^{-10}	d
$Ar^++Al\rightarrow Al^++Ar$	1.0×10^{-9}	d
$Ar^++Al^*\rightarrow Al^++Ar$	1.0×10^{-9}	d
$Ar^++Ar\rightarrow Ar+Ar^+$	1.0×10^{-9}	d
$Ar^++Ar^*\rightarrow Ar+Ar^+$	1.0×10^{-9}	d
$Al^++Al\rightarrow Al+Al^+$	1.0×10^{-9}	d
$Al^++Al^*\rightarrow Al+Al^+$	1.0×10^{-9}	d

[a]In the FKS, all excitations of Ar are lumped into Ar*, which is effectively Ar ($4s$), and all excitations of Al are lumped into Al*, which is effectively Al ($4s$).
[b]The rate coefficients are calculated from electron energy distribution obtained in the EETM.
[c]Rate coefficient for superelastic collisions are obtained by detailed balance.
[d]Estimated.

III. VALIDATION

The HPEM IMPVD algorithms were validated by comparing computed results with experimental measurements from Dickson and Hopwood.[8] A schematic of the ICP reactor is shown in Fig. 2. The diameters of the target and the rf induction coils are 7.5 and 15.0 cm, respectively. The upper turn of the two-turn coil (separation 2.5 cm) is 4 cm from the target. The diameter of the substrate is 22 cm. The distance between the target and the substrate is 12 cm. The operating conditions are 400 W ICP power, 240 W magnetron power, 30 mTorr Ar buffer gas, and 150 sccm gas flow. The ampli-

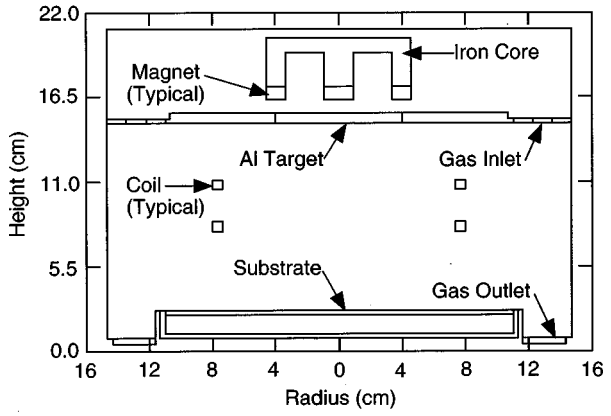

FIG. 2. Schematic of the IMPVD reactor for validation of the model. The reactor has a magnetron on top and an Al target and coils that are immersed in the plasma.

tude of the 13.56 MHz rf potential on the coils was specified to be 100 V. The secondary electron coefficient was specified to be 0.35.

The predicted electron temperature is shown in Fig. 3(a). The electron temperature is high throughout the reactor, about 4.0 eV, typical of an ICP plasma. The maximum electron temperature of 4.5 eV occurs below the magnetron, caused by the emission of energetic secondary electrons from the magnetron target and joule heating due to current focused through the cusp. Another local maximum of 4.1 eV occurs around the two ICP coils where most of the ICP power is deposited because of the short skin depth.

The predicted Al densities (sum of thermalized Al and in-flight Al) are shown in Fig. 3(b). The Al density is 7.0 $\times 10^{11}\,\mathrm{cm}^{-3}$ below the target where the source due to sputtering is large, then rapidly decreases toward the wafer due to thermalization and diffusion. The Al density is nearly constant at $10^{11}\,\mathrm{cm}^{-3}$ from 2 to 7 cm above the wafer, between the coils, and the center line. This region of constant Al density results from coil sputtering, which significantly contributes to the Al density. The predicted Al^+ and Ar^+ densities are shown in Figs. 3(c) and 3(d). Compared to the predicted Al density, the Al^+ density peaks nearer the center of the reactor due to the loss of ions to the target and the substrate, and the major ionization source being near the coils. The Ar^+ density profile is similar to the Al^+ density profile, except for being about 10 times higher.

The predicted magnetron current and voltage are 0.94 A and 255 V, respectively, which agree well with experimental values of 1.0 A and 240 V. The predicted Al density is 1.1 $\times 10^{11}\,\mathrm{cm}^{-3}$ at 8–10 cm below the target at a radius of 4 cm which agrees well with the experimental values of 1.0–1.5 $\times 10^{11}\,\mathrm{cm}^{-3}$ obtained from deposition rates.[8] The predicted ionization ratio $[Al^+/(Al^+ + Al)]$.

10 cm below the target at a radius of 4 cm is 17% while the experimental values are 10%–15%. The predicted ion fraction of the metal flux to the wafer (12 cm below target, at a radius of 4 cm) is 74%, which agrees well with the experimental value of 70%.

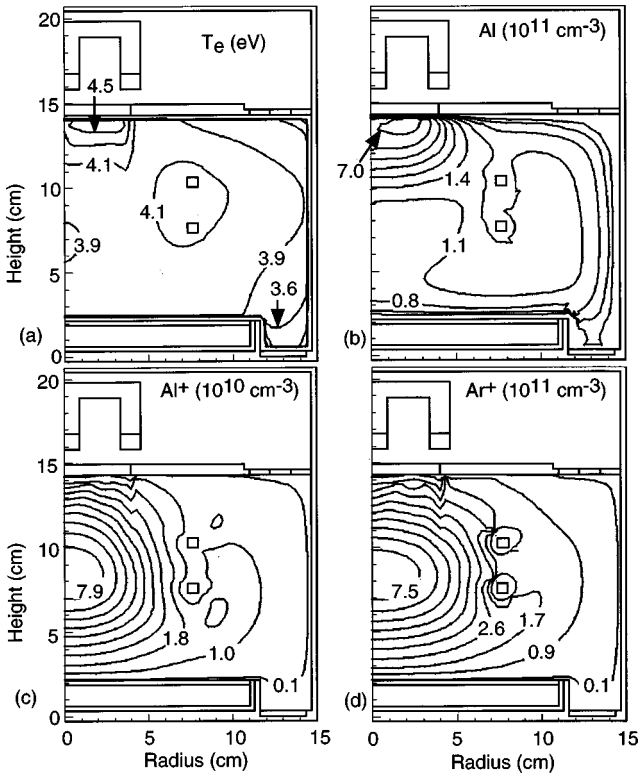

FIG. 3. Predicted plasma properties for the case of model validation: (a) electron temperature, (b) Al density, (c) Al^+ density, and (d) Ar^+ density. The electron temperature peaks below the magnetron. The Al density (including both thermal and nonthermal Al atoms) decreases from the target to the substrate with there being a contribution to the density from sputtering of the coils. Both Al^+ and Ar^+ densities peak at the center of the reactor.

IV. SPUTTER HEATING

Given this validation, we turned our attention to the more industrially relevant IMPVD reactor schematically shown in Fig. 4(a). The rf ICP power is supplied through coils outside the plasma region using a Faraday shield.[29] The purpose of the Faraday shield is to prevent the blocking of ICP power into the plasma due to metal deposition on the reactor side wall. Details of the geometry of the Faraday shield are not shown here. Computationally, the azimuthal electric field is allowed to simply propagate through the Faraday shield. The advantages of the external coil are the elimination of coil erosion due to sputtering and simplification of the interpretation of the results. The diameters of the target and the substrate are 22 and 21 cm, respectively. The distance between the target and the substrate is 15 cm. The base case operating conditions are 0.5 kW ICP power, 1.0 kW magnetron power, 30 V rf at 13.56 MHz on the substrate, and 30 mTorr Ar.

The static magnetic field properties are shown in Figs. 4(b) and 4(c). The field is 250 G below the target, midway between the magnet poles. The field decays away from the target, and is $\approx$10 G above the substrate. The magnetic field lines form a cusp below the target, confining electrons and focusing ion fluxes into the target. (The peak rf magnetic field strength from the coil current is only 5–10 G, and so it does not appreciably affect electron transport or confinement.) The magnetron confinement is demonstrated by the

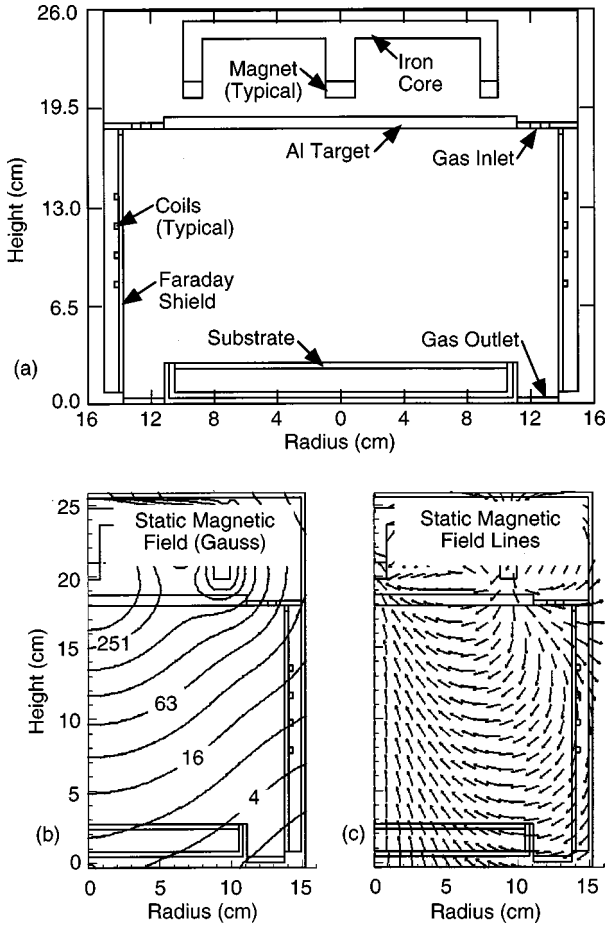

FIG. 4. Reactor and magnetic field characteristics for the sputter heating study: (a) schematic of an IMPVD reactor with external coils and a Faraday shield, (b) static magnetic field, and (c) magnetic field vectors.

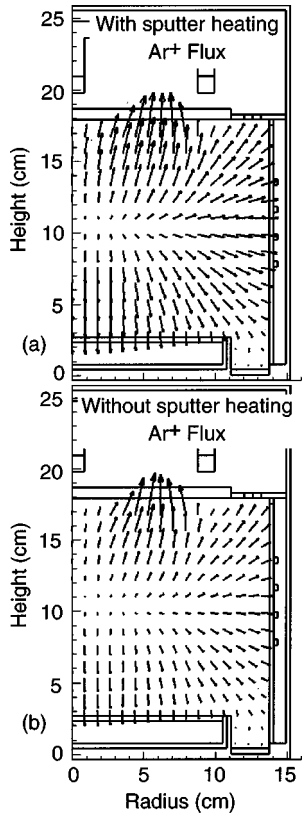

FIG. 5. Ar^+ fluxes (a) with and (b) without sputter heating for the base case. The Ar^+ fluxes are at a maximum in the cusp of the magnetic field.

Ar^+ fluxes, shown in Fig. 5, with and without sputter heating. The Ar^+ flux accounts for 90% of the total flux. In both cases, the Ar^+ flux to the target is a maximum [$\approx 10^{17}\,cm^{-2}\,s^{-1}(160\,mA/cm^2)$] in the cusp of the magnetic field. Outside the magnetron confinement region, the Ar^+ flux with sputter heating is larger than without sputter heating since the Ar^+ density is larger with sputter heating, as discussed below. For 1 kW magnetron power, the target voltage with and without sputter heating is 178 and 168 V, respectively. In spite of the fact that the ion density in the bulk plasma increases, there is a small decrease in ion flux to the target with sputter heating, so more voltage is required to maintain the same magnetron power with the lower ion current.

The Ar and Ar^+ densities are shown in Fig. 6, with and without sputter heating. The Al and Al^+ densities are shown in Fig. 7. In both cases, the Ar^+ density peaks near the center of the reactor due to the large ionization source from the ICP coils. The Ar^+ temperature at the center of the plasma is 1200 K with sputter heating and 2900 K without sputter heating. Since the plasma is collisional and Ar^+ is accelerated by the electric field approaching the target and the substrate, the Ar^+ temperature is high (1–2 eV) near the target and the substrate. The Ar^+ density with sputter heating is $\approx$50% higher than without, except below the target and near the outlet. Sputter heating has the effect of quenching the Ar^+ temperature and increasing the Ar^+ density. Without sputter heating there is a local maximum of Ar^+ density below the target, which dissipates with sputter heating, an effect discussed below.

The Ar density (Al has only a 0.1% mole fraction) without sputter heating is a minimum 2 cm below the target largely due to heating resulting from power transfer during symmetric charge exchange as ions are accelerated towards the target. The gas temperature at that location, shown in Fig. 8, is 820 K. With sputter heating, the minimum Ar density is directly below the target where sputtered and reflected atoms slow down and is smaller by 30% compared to that without sputter heating. The gas temperature is 1150 K below the target with sputter heating. In both cases, the minimum Ar density occurs below the target where the ion flux to the target is maximum. This is expected since more incident ions lead to more sputtering and more reflected neutrals, which results in more energy and momentum transfer and more gas rarefaction. The concentration of ion current due to the magnetron effect also leads to more charge exchange heating.

In the absence of sputter heating, the gas density below the target is higher, which leads to a shorter stopping distance for secondary electrons for ionization, a more severe gradient for the electron temperature (see below), and a shorter mean free path for ions produced near the target. As a result, there is a larger local maximum in the ion density below the target. With sputter heating, the gas is more rarefied below the target, producing longer mean free paths and

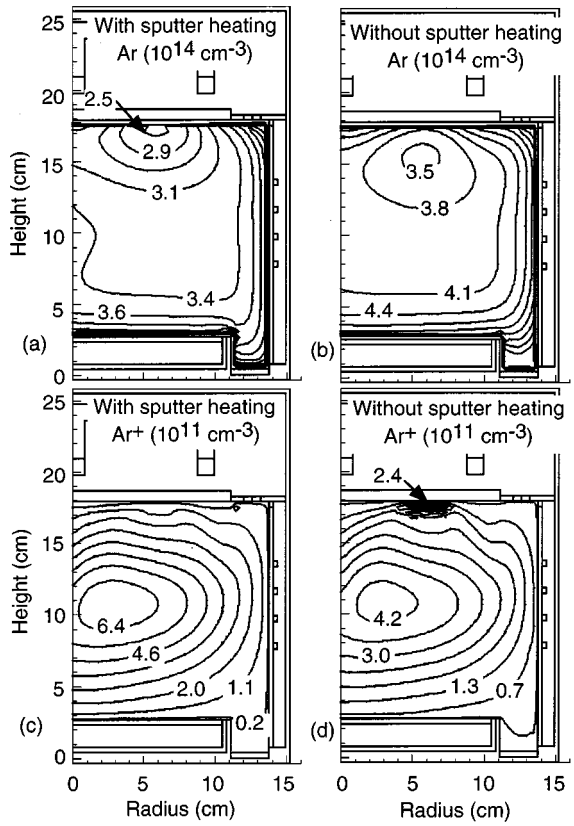

FIG. 6. Predicted Ar and Ar^+ densities with and without sputter heating. (a) Ar with sputter heating, (b) Ar without sputter heating, (c) Ar^+ with sputter heating, and (d) Ar^+ without sputter heating. The minimum Ar densities are below the target, and the maximum Ar^+ densities are near the center of the plasma.

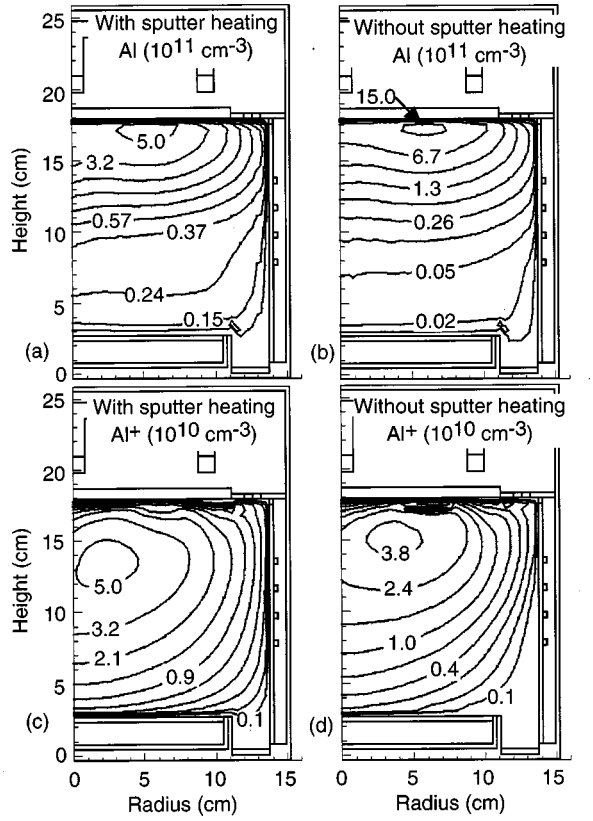

FIG. 7. Predicted Al and Al^+ densities with and without sputter heating. (a) Al with sputter heating, (b) Al without sputter heating, (c) Al^+ with sputter heating, and (d) Al^+ without sputter heating. The Al densities decrease from the target to the substrate, and the maximum Al^+ densities are several cm below the target.

a more diffuse plasma. For incident ions of 180 eV, the average kinetic energies of the reflected neutrals and sputtered atoms are both about 8 eV. The yield of the $Ar^+ - Al$ pair is about 0.4, compared to an effective yield of 0.9 for the reflected energetic neutrals. Hence, the reflected neutrals contribute about two thirds of the gas heating.

The more important effect of sputter heating is the significant gas rarefaction throughout the reactor, not just below the target. For example, the Al density is maximum below the target where sputtered Al atoms initially undergo collisions with the buffer gas, and then decreases toward the substrate (see Fig. 7). The maximum Al density with sputter heating is only one third that without heating, although its gradient to the substrate is smaller. This reduction in the Al peak is due to the longer mean free path for slowing and longer diffusion length with the additional rarefaction. Since the magnetron power is constant, the sputtered atom fluxes and the total Al inventory sputtered should be approximately the same in both cases. This inventory of Al atoms is redistributed in the reactor by gas rarefaction, producing less severe gradients with sputter heating. The Al^+ density without sputter heating is maximum 3 cm below the target, compared to 5 cm below the target with sputter heating. This is largely a reflection of the shift in the Al density. In addition, the mean free path for Al ionization increases as the gas becomes more rarefied while Al^+ below the target is depleted by the ion current to the target, which help to move the Al^+ density peak away from the target.

The electron temperature is shown in Fig. 9 with and without sputter heating. In both cases, the maximum electron temperature is below the target and next to the ICP coils, and reflects the local sources of heating. The maximum electron temperature is 3.8 eV with sputter heating, 1 eV lower than the 4.8 eV without sputter heating. The electron temperature also decreases throughout the reactor with sputter heating, consistent with the experimental observations from Dickson *et al.*[7]

The Al flux to wafer is shown in Fig. 10 with and without sputtering. The total depositing flux consists of Al^+, Al^*, thermal Al, and nonthermal Al. The source of thermal Al atoms is the sputtered Al atoms which have slowed to twice the local temperature. Nonthermal Al refers to the unthermalized sputtered Al atoms. The Al^* contribution is negligible because its density is depleted by rapid radiative relaxation, de-excitation, and ionization. Since the mean free path for sputtered Al atoms is on the order of a centimeter, most of the sputtered atoms undergo many collisions and therefore are thermalized when they reach the substrate. Hence, the nonthermal Al contribution is also negligible.

Since most sputtered Al atoms are thermalized several cm below the target, the thermalized Al atoms have ample opportunity to charge exchange with Ar^+ and to undergo electron impact ionization. Consequently, the majority of the

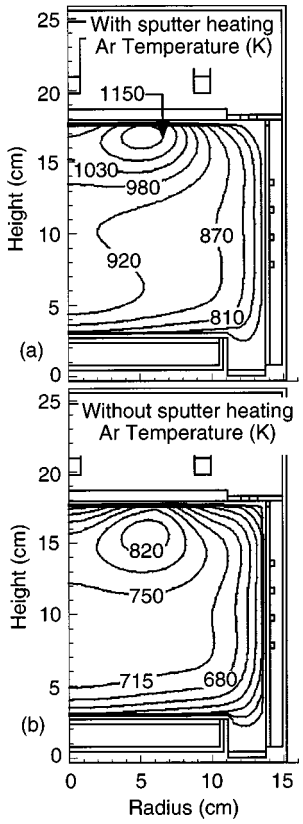

FIG. 8. Predicted Ar temperature (a) with and (b) without sputter heating for the base case. The Ar temperatures peak below the target where charge exchange and sputter heating are maximum.

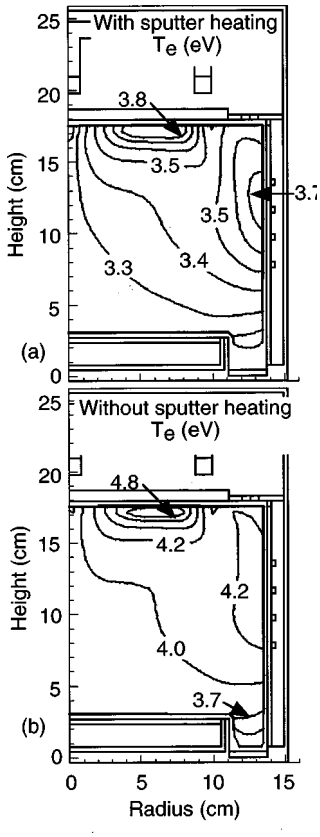

FIG. 9. Predicted electron temperature (a) with and (b) without sputter heating for the base case. The electron temperature peaks below the target and near the rf coils due to magnetron heating and the deposition of power in the skin depth.

depositing metal flux consists of Al^+. The ionization fraction of the depositing flux is 95% at the center and 89% at the wafer edge without sputter heating, and 86% at the center and 67% at the wafer edge with sputter heating. Since sputter heating rarefies the background gas and increases the mean free path for Al transport, the opportunity for ionization collisions decreases for Al, and so the ionization fraction also decreases. The effect is similar to operating at a lower pressure, where it is observed that ionization fractions decrease.[30] The thermal Al and Al^+ depositing flux with sputter heating is eight and two times that without sputter heating. This difference is caused by the redistribution and slower decay of the Al species toward the wafer due to gas rarefaction and by there being fewer losses of backscattered Al atoms to the target. The total depositing Al flux with sputter heating is 2.3 times that without sputter heating. Hence, including sputter heating has the effect of decreasing the ionization fraction of the depositing metal flux and increasing the magnitude of the depositing metal flux under typical operating conditions.

The minimum and reactor-averaged Ar densities are shown in Fig. 11 as a function of ICP and magnetron powers. Without magnetron power, the minimum Ar density is about $4.3\times10^{14}\,\mathrm{cm}^{-3}$ at 0.5 kW ICP, and the maximum gas temperature is 690 K [see Fig. 11(c)]. This is the ''base heating'' (above an ambient wall temperature of 350 K) due only to ICP power. The minimum Ar density decreases by 43% with 0.5 kW ICP power as the magnetron power is increased from

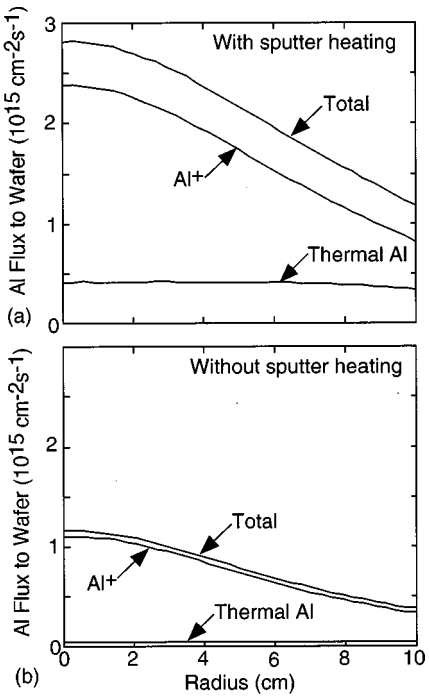

FIG. 10. Depositing Al flux to wafers (a) with and (b) without sputtering for the base case. The ionization fraction of the depositing flux decreases with sputter heating while the magnitude of the flux increases.

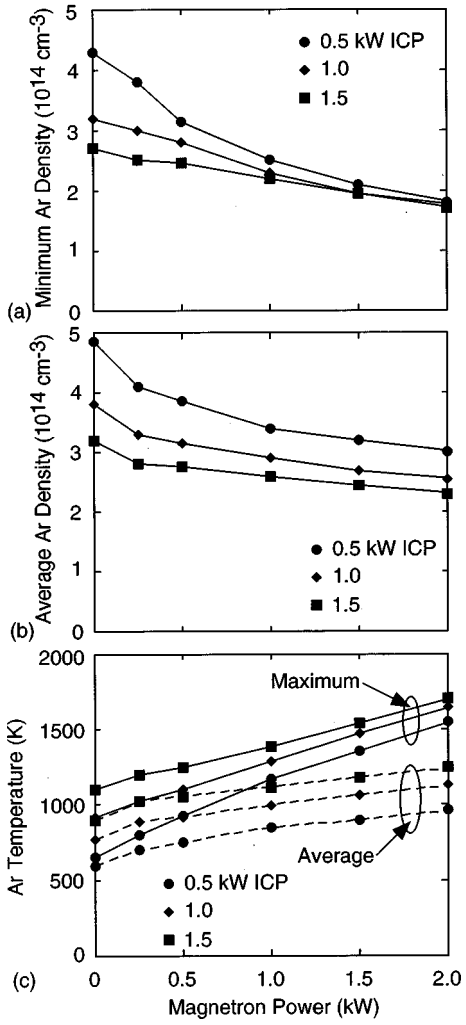

FIG. 11. Ar densities and temperatures with sputter heating as a function of ICP and magnetron power. (a) Minimum Ar density, (b) reactor-averaged Ar density, and (c) maximum and reactor-averaged Ar temperatures. The Ar densities decrease (and temperatures increase) with increasing ICP power (due primarily to charge–exchange heating) and magnetron power (due primarily to sputter heating).

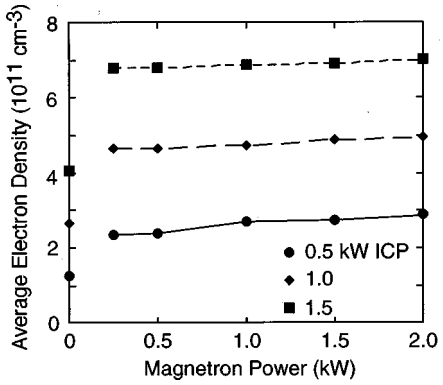

FIG. 12. Reactor-averaged electron density with sputter heating as a function of ICP and magnetron power. The electron density increases significantly with the addition of metal species, and then saturates with increasing magnetron power.

0.5 to 2.0 kW, which generally agrees with the 40% reduction of Ar density observed by Rossnagel under similar operating conditions for a Cu target.[6] At constant ICP power, the minimum Ar density decreases monotonically with increasing magnetron power, which is expected because more magnetron power results in more sputtering, more sputter heating, and more rarefaction. As the magnetron power increases, densities are less sensitive to ICP power, partly because the contribution to heating by ICP power becomes an increasingly smaller fraction of the total.

The minimum gas density and the peak gas temperature occur right below the target. There are two effects which tend to saturate the minimum gas density (and the maximum gas temperature) as the magnetron power increases. The first is that, as the power increases and the gas rarefies, the mean free path for slowing of the sputtered atoms and reflected neutrals increases, and slowing occurs in a larger volume. The power density (W/cm^3) producing sputter heating therefore tends to saturate. The second is that, as the gas temperature increases at higher power, the heat transfer from the hot gas below the target to the target surface (held at 350 K here) also increases. This heat transfer somewhat limits the gas temperature, and hence gas rarefaction, below the target.

The reactor-averaged Ar density also monotonically decreases with increasing magnetron power. However, since the cold gas near the side walls is weighted more in volume and is closer to the ICP source, there is a larger effect of ICP power. The maximum Ar temperature (corresponding to the minimum Ar density) and the reactor-averaged Ar temperature (corresponding to the reactor-averaged Ar density) are shown in Fig. 11(c). The maximum Ar temperature ranges from 700 to 1700 K, while the average Ar temperature ranges from 600 to 1250 K. Both Ar temperatures increase with increasing magnetron and ICP power. In general, increases in temperature due to ICP power result from charge–exchange heating while increases in gas temperature due to magnetron power result from sputter heating.

The reactor-averaged electron density is shown in Fig. 12 as a function of ICP and magnetron power. Average electron densities are $2\times10^{11}\,\mathrm{cm}^{-3}$ for 0.5 kW ICP to $7\times10^{11}\,\mathrm{cm}^{-3}$ for 1.5 kW ICP. As with conventional ICP tools, the electron density increases nearly linearly with power.[31] The electron density increases significantly when the magnetron power is increased from zero. The addition of magnetron power produces sputtering, and hence introduces low-ionization potential Al atoms into the plasma. The metal atoms are more easily ionized by both electron impact and Penning reactions with Ar^*, which increase the electron density. As the magnetron power continues to increase, gas rarefaction due to sputter heating increases the mean free path for Al ionization, thus reducing the ionization fraction of Al atoms, as suggested by the depositing Al flux seen in Fig. 10(a). This rarefaction tends to reduce the additional ionization which one might otherwise obtain from the increasing magnetron power. Note that for a magnetron power of 1.0 kW (with 0.5 kW ICP), the power dissipated in ion acceleration is 740 W or 74% of the total, so the amount of power available for additional ionization is only 240 W.

V. CONCLUDING REMARKS

A model was developed to investigate sputter heating in IMPVD reactors. The model accounts for ion-energy-dependent sputter yield, kinetic energy of the sputtered atoms and reflected neutrals, and the transfer of momentum and energy from the sputtered metal atoms and the reflected neutrals to the background gas atoms. Comparisons between experimental data and model predictions for Al IMPVD indicate that the sputter model reasonably reproduces the voltage–current characteristic of the magnetron and the transport of the sputtered atoms in the secondary plasma. We found that sputter heating significantly rarefies the buffer gas, thus increasing the mean free path for sputtered metal transport and redistributing the metal species in the reactor. Consequently, sputter heating decreases the ionization fraction of the depositing metal flux, but increases its magnitude. As the power increases, the minimum gas density below the target is limited by thermal transfer from the hot gas to the cold target and a lower specific power deposition resulting from the rarefaction. The electron density increases significantly when a small amount of metal atoms with low ionization potential is introduced into the plasma. However, the electron density saturates with increasing magnetron power because gas rarefaction tends to decrease the ionization fraction of the metal atoms. At constant magnetron power, the electron density increases linearly with the ICP power under the operating conditions in this study.

ACKNOWLEDGMENTS

This work was funded by Semiconductor Research Corporation and Tokyo Electronics of Arizona. The authors wish to thank Professor David Ruzic (Department of Nuclear Engineering, University of Illinois at Urbana–Champaign) for performing TRIM calculations for the kinetic energy of reflected neutrals. They also thank Professor Jeff Hopwood (Department of Electrical and Computer Engineering, Northeastern University) and Michael Grapperhaus of Tokyo Electronics for helpful discussions on sputter heating.

[1] S. M. Rossnagel, Semicond. Int. **21**, 99 (1996).
[2] S. M. Rossnagel and J. Hopwood, J. Vac. Sci. Technol. B **16**, 499 (1998).
[3] C. Ryu, H. Lee, K. W. Kwon, A. L. S. Loke, and S. S. Wong, Solid State Technol. **42**, 53 (1999).
[4] D. W. Hoffman, J. Vac. Sci. Technol. A **3**, 561 (1985).
[5] Z. C. Lu, J. E. Foster, T. G. Snodgrass, J. H. Booske, and A. E. Wendt, J. Vac. Sci. Technol. A **17**, 840 (1999).
[6] S. M. Rossnagel, J. Vac. Sci. Technol. A **6**, 19 (1988); J. Vac. Sci. Technol. B **16**, 3008 (1998).
[7] M. Dickson, F. Qian, and J. Hopwood, J. Vac. Sci. Technol. A **15**, 2161 (1997).
[8] M. Dickson and J. Hopwood, J. Vac. Sci. Technol. A **15**, 2307 (1997).
[9] G. M. Turner, J. Vac. Sci. Technol. A **13**, 2161 (1995).
[10] V. V. Serikov and K. Nanbu, J. Appl. Phys. **82**, 5948 (1997).
[11] M. J. Grapperhaus, Z. Krivokapic, and M. J. Kushner, J. Appl. Phys. **83**, 35 (1998).
[12] M. J. Grapperhaus and M. J. Kushner, J. Appl. Phys. **81**, 569 (1997).
[13] N. Masunami, Y. Yamamura, Y. Itikawa, N. Itoh, S. Kazumata, S. Miyagawa, K. Morita, R. Shimizu, and H. Tawara, At. Data Nucl. Data Tables **31**, 1 (1984).
[14] Y. Yamamura, N. Matsunami, and N. Itoh, Radiat. Eff. **71**, 65 (1983).
[15] J. Lindhard and M. Scharff, Phys. Rev. **124**, 128 (1961).
[16] M. W. Thompson, Philos. Mag. **18**, 377 (1968).
[17] V. V. Serikov and K. Nanbu, J. Vac. Sci. Technol. A **14**, 3108 (1996).
[18] M. A. Lieberman and A. J. Litchtenberg, *Principles of Plasma Discharges and Material* (Wiley, New York, 1994), p. 253.
[19] D. N. Ruzic (private communication).
[20] D. N. Ruzic, Nucl. Instrum. Methods Phys. Res. B **47**, 118 (1990).
[21] A. Bogaerts, M. van Straaten, and R. Gijbels, J. Appl. Phys. **77**, 1868 (1995).
[22] M. Hayashi, Nagoya Institute of Technology Report No. IPPJ-AM-19 (1991).
[23] K. Tachibana, Phys. Rev. A **34**, 1007 (1986).
[24] D. Rapp and P. Englander-Golden, J. Chem. Phys. **43**, 1464 (1965).
[25] R. H. McFarland and J. D. Kinney, Phys. Rev. **137**, A1058 (1965).
[26] E. McGuire (private communication).
[27] L. L. Shimon, E. I. Nepiipov, and I. P. Zapesochnyi, Sov. Phys. Tech. Phys. **20**, 434 (1975).
[28] L. Virens, Phys. Lett. **8**, 260 (1964).
[29] R. Bayer, A. D. Lantsman, and J. A. Seirmarco, U.S. Patent No. 5,569,363 (filed 1996).
[30] W. Wang, J. Foster, T. Snodgrass, A. E. Wendt, and J. H. Booske, J. Appl. Phys. **85**, 7556 (1999).
[31] J. H. Keller, Plasma Sources Sci. Technol. **5**, 165 (1996).